

1 **Deposition of light-absorbing particles in glacier snow of the Sunderdhunga Valley, the**
2 **southern forefront of Central Himalaya**

3

4 Jonas Svensson^{1,2}, Johan Ström³, Henri Honkanen⁴, Eija Asmi¹, Nathaniel B. Dkhar⁵, Shresth
5 Tayal^{5,6}, Ved P. Sharma^{5,6}, Rakesh Hooda¹, Matti Leppäranta⁴, Hans-Werner Jacobi², Heikki
6 Lihavainen^{7,1}, Antti Hyvärinen¹

7 1 Atmospheric Composition Research, Finnish Meteorological Institute, Helsinki, Finland

8 2 Université Grenoble Alpes, CNRS, IRD, INP-G, IGE, Grenoble, France

9 3 Department of Environmental Science, Stockholm University, Stockholm, Sweden

10 4 Institute for Atmospheric and Earth System Research, Faculty of Science, University of Helsinki,
11 Helsinki, Finland

12 5 The Energy and Resource Institute, (TERI), New Delhi, India

13 6 TERI School of Advanced Studies (TERI SAS), New Delhi, India

14 7 Svalbard Integrated Arctic Earth Observing System, Longyearbyen, Norway

15

16 Correspondence to: jonas.svensson@fmi.fi

17

18 **Abstract**

19 Anthropogenic activities on the Indo-Gangetic Plain emit vast amounts of light-absorbing particles
20 (LAP) into the atmosphere, modifying the atmospheric radiation ~~scheme~~ **state**. With transport to the
21 nearby Himalayan mountains and deposition to its surfaces the particles contribute to glacier and
22 snowmelt via darkening of the highly reflective snow. The Central Himalayas have been identified as a
23 region where LAP are especially pronounced in glacier snow, but still remain a region where
24 measurements of LAP in the snow are scarce. Here we study the deposition of LAP in five snow pits
25 sampled in 2016 (and one from 2015) **within one km from each other** from two glaciers in the
26 Sunderdhunga valley, state of Uttarakhand, India, Central Himalaya. The snow pits display a distinct
27 ~~melt~~ **enriched LAP** layer interleaved by younger snow above, and older snow below. The LAP exhibit
28 a distinct vertical distribution in these different snow layers. For the analyzed elemental carbon (EC),
29 the younger snow layers in the different pits show similarities, ~~and~~ **which** can be characterized by a
30 deposition constant of about $50 \mu\text{g m}^{-2} \text{ per mm}^+ \text{ snow water equivalent (SWE)}$ while the old snow
31 layers also indicate similar values, ~~and can be described with~~ **by** a deposition constant of roughly 150
32 $\mu\text{g m}^{-2} \text{ per mm}^+ \text{ SWE}$. The ~~melt~~ **enriched LAP** layer, contrarily, display no similar trends between the
33 pits. Instead, it is characterized by very high amounts of LAP, and differ in orders of magnitude for
34 concentration between the pits. The ~~melt~~ **enriched LAP** layer is likely a result of strong melting that
35 took place during the summers of 2015 and 2016, **as well as possible lateral transport of LAP**. The

36 mineral dust fractional absorption is slightly below 50 % for the young and old snow layer, whereas ~~it~~
37 ~~the melt layer~~ is the dominating light absorbing constituent **in the enriched LAP layer**, thus, highlighting
38 the importance of dust in the region. Our results indicate the problems with complex topography in the
39 Himalaya, but nonetheless, can be useful in large-scale assessments of LAP in Himalayan snow.

40 1 Introduction

41 Aerosol particles in the Indo-Gangetic Plain (IGP) are produced in great mass and number. Being
42 especially prominent in the pre-monsoon season, a large fraction of the airborne aerosols are
43 carbonaceous particles, consisting of organic carbon (OC) and black carbon (BC). Originating from the
44 combustion of fossil fuels and biomass, the particles form the atmospheric brown cloud—known to
45 modify the atmospheric radiation ~~scheme~~ **state** (Lau et al., 2006; Menon et al., 2010; Ramanathan and
46 Carmichael, 2008). Through air mass transport the aerosol can be conveyed and lifted from the IGP to
47 its northern barrier, the mountains of Himalaya (e.g. Hooda et al., 2018; Kopacz et al., 2011;
48 Raatikainen et al., 2014; Zhang et al., 2015). Covered with vast amounts of snow and ice, the Himalayan
49 cryosphere is affected by the deposition of carbonaceous aerosol onto its surface (e.g. He et al., 2018;
50 Jacobi et al., 2015; Ménégoz et al., 2014; Xu et al., 2009). This is due to the particulates and especially
51 BC effectiveness in reducing the snow albedo (Warren and Wiscombe, 1980), which ultimately leads
52 to accelerated snow melt (Flanner et al., 2007; Jacobi et al., 2015; Jacobson, 2004; Ming et al., 2012).

53

54 In addition to BC and OC, other particles such as mineral dust (MD) and snow microbes (collectively
55 known as light-absorbing particles (LAP)) are also of importance in reducing snow albedo (e.g. Skiles
56 et al. 2018). In Himalayan snow and ice, the LAP content has been shown to vary significantly, both
57 spatially and temporally (e.g. see review by Gertler et al., 2016). Further, an extensive compilation of
58 BC measurements in snow over the Tibetan Plateau is presented in the supplement of He et al. (2018),
59 with concentrations ranging from 1 to 3600 ppb_w in the region termed as Himalaya. In addition to long
60 range transported LAP, local sources within the Tibetan plateau have also been documented to be
61 significant in some regions (e.g. Li et al., 2016), creating several different sources of LAP in the snow.
62 Varying meteorology and terrain induced exchange processes (advection and turbulence) in the
63 mountains further complicates the interplay between the atmospheric deposition of LAP and the snow
64 surfaces.

65

66 ~~Observations are further supported by modeling studies, which indicate~~ **Recent modeling studies have**
67 **reported analogous results**, indicating certain sub-regions of the Himalaya to be especially vulnerable
68 to LAP deposition. Santra et al. (2019) ~~recently~~ simulated the BC impact on snow albedo and glacier
69 runoff in the Hindu Kush-Himalaya region. The authors identified a hot-spot zone for BC in the vicinity
70 of Manora peak, located in the Indian state of Uttarakhand, central Himalaya (also sometimes called
71 western Himalaya depending on classification). The BC induced a greater albedo reduction on glacier
72 snow in the vicinity of this hot spot area compared to other areas in the Hindu Kush-Himalayan area.
73 Similarly, another modeling study simulated the impact of LAP on High Mountain Asia snow albedo
74 and its associated forcing and identified the same general area as a region where snow is especially
75 affected by LAP-caused snow darkening (Sarangi et al., 2019). Both of these studies (as well as the

76 work of He et al., 2018) emphasized the need for more *in situ* measurements of LAP in the snow of this
77 region of the Himalaya.

78

79 Previously, we reported in Svensson et al. (2018) the measured LAP concentrations and properties in
80 the snow from two glaciers in the Sunderdhunga valley, located in Uttarakhand, India, central Himalaya.
81 While we mainly focused on the surface snow layer and characterizing the LAP, results from one 1.2
82 m deep snow pit were also presented. Based on the LAP concentration profile and pit stratigraphy, the
83 pit was estimated to represent 5 seasons. Newly sampled snow pits have since then been analyzed from
84 the same two glaciers, along with available automatic weather station (AWS) data from the same valley.
85 Here we revisit the previous interpretation of the published pit (in Svensson et al., 2018), and report the
86 results of our newly sampled snow pits. By comparing the BC profiles among 6 pits we aim at
87 quantifying the deposition of elemental carbon (EC; used here as a proxy for BC) in this area of the
88 Himalaya. In addition, we explore the relative contribution of MD to LAP in the different pits.

89

90 2 Methodology

91 2.1 Glaciers snow sampling and filtration

92 Snow was collected on Bhanolti and Durga Kot glaciers during a field campaign in the Sunderdhunga
93 valley (located in the Bageshwar district) in October of 2016. The two glaciers are positioned adjacent
94 to each other in a general northeast-southwest orientation (cf. Fig. 1) on the southern fringe of the
95 Himalayan mountain range and are further described in Svensson et al. (2018). Local emissions of
96 carbonaceous aerosol in the Sunderdhunga valley are very limited. The valley is not accessible by car
97 and the glaciers are at a three to four-day hike from the nearest road. On route to the glaciers the last
98 settlement is Jatoli, located in a river valley at an elevation of 2400 m. a.s.l. about 10 km southeast in a
99 perpendicular orientation to the glacier valley. Biomass burning is a common practice for cooking and
100 heating in Jatoli, thus some emissions from the village may enter the glacier valley. It is expected,
101 however, that the majority of carbonaceous particles in the glacier valley originates from regional and
102 long-distance transport. The relatively low elevation span as well as the glaciers' position on the
103 southern slopes of the Himalayan mountains nonetheless, make them more prone to LAP deposition
104 compared to other glaciers in the Himalaya and Tibetan plateau. Previous studies have reported elevated
105 LAP content in lower elevation snow for Himalayan glaciers (e.g. Ming et al., 2013), and higher
106 concentrations of LAPs in glaciers on the southern edge of the Himalaya (e.g. Xu et al., 2009).

107

108 On Durga Kot glacier two snow pits (hereafter Pit A and B; Fig. 1) were dug in the vicinity of each
109 other (~20 m) in an reachable area of the percolation zone of the glacier. Bhanolti glacier was more
110 easily accessible, and the three excavated snow pits (hereafter Pit C, D, E; Fig. 1) were spread out over
111 a greater distance (~500 m) on the glacier (see table 1 and Fig. 1 for additional information). The depth

112 of the pits depended on the level at which a hard layer was found, and digging could not be further
113 conducted **with the reinforced shovels with a sharpened edge**. The deepest snow pit that was analyzed
114 previously in Svensson et al. (2018), referred to as pit 5 in that study, is from Bhanolti glacier in
115 September of 2015, and we denote as Pit F in the subsequent sections of this manuscript. As for the
116 other pits from 2016, the depth of Pit F was governed by the depth at which the hard layer was
117 encountered.

118
119 Three distinctly different colored snow layers could be observed repeating in all but one of the year
120 2016 pits: a relatively thin (on the order of centimeters) very dark layer was ~~separated by~~ **wedged in-**
121 **between** white snow above and more grey appearing snow below (**See for e.g. pits B and D in Fig. S1a-**
122 **b**). Due to this stratigraphy, we hereafter simply refer to the whitest snow as young snow, the darkest
123 layer as the ~~melt~~ **enriched LAP** layer, and the grey snow as old snow. Representative samples ranging
124 from 3 to 10 cm thick layers were taken throughout each pit for analysis of LAP. Snow density
125 measurements were conducted with a snow density kit in the upper part of the pits (in 5 cm increments)
126 by weighing the known volume of the sampler filled with snow. The observed densities ranged between
127 0.29 and 0.46 g cm⁻³ (see table 1 for details). Density measurements were not possible below the ~~melt~~
128 **enriched LAP** layer due to the hard snow. For these layers the density was assumed 0.5 g cm⁻³ (to
129 represent aged snow) in our further analyzes. Snow density measurements were not conducted for Pit
130 F, and we assigned a density of 0.35 g cm⁻³ for the top layer (0-3 cm; similar to observations made in
131 2016), followed by 0.4 g cm⁻³ between 3-10 cm depth, and 0.5 g cm⁻³ for all layers below 10 cm. Since
132 the snow samples could not be transported in a solid phase back to the laboratory, they were melted and
133 filtered at the nearby base camp using the same principles as in Svensson et al. (2018). Filters were
134 transported back to the analysis laboratory in petri slides.

135

136 2.2 Meteorological observations

137 In September 2015 an AWS was installed next to the glacier ablation zone of Durga Kot (Fig. 1) about
138 1.5 km northwards at an elevation below the snow sampling sites. The AWS is equipped with
139 instruments for air temperature, relative humidity (**HC2S3-L Temperature and relative humidity probe**
140 **manufactured by Rotronic, with 41303-5A Radiation shield**), shortwave (SW) and longwave (LW)
141 radiation (**upward** and **downward**) (**CNR4 Four-component net radiometer manufactured by Kipp &**
142 **Zonen**), wind speed and direction (**05103-L Wind monitor manufactured by R. M. Young**), and snow
143 depth (Campbell Scientific SR50**A-L** Ultrasonic Distance Sensor). In this paper we use the snow depth
144 data between September 2015 and September 2017 to estimate the local precipitation. The original snow
145 depth data, logged once every 10 minutes was filtered to daily resolution by applying a moving median
146 window of 24 hours and for the noon value of each day in further analyzes. This filtering removed much
147 of the signal noise. However, before this filtering was applied the data was reduced using several logical

148 conditions such as: the incoming SW radiation is greater than outgoing SW radiation (to remove errors
149 due to sensors covered by snow), and the surface albedo is greater than 0.2 (to ensure snow cover **as the**
150 **ground albedo was measured at 0.17**). Finally, the consistency between the daily albedo and snow depth
151 was inspected using data presented in Figure S42a. Each day the snow depth increased was interpreted
152 as precipitation, and to arrive at an estimate of the snow water equivalent (SWE), the fresh snow density
153 is assumed to be 100 kg m^{-3} (Helfricht, et al., 2018). The solid precipitation derived based on the
154 cumulative SWE is presented in Figure S42b.

155

156 2.3 Filter analysis

157 The analysis of filters followed the procedure in Svensson et al. (2018), with transmission
158 measurements coupled with thermal-optical analysis. According to the measurement nomenclature
159 (Petzold et al., 2013), the carbonaceous constituents measured are EC and OC. The measurement
160 method briefly follows the procedure of placing a filter punch in a custom-built particle soot absorption
161 photometer (PSAP) to measure the transmittance (at $\lambda = 526 \text{ nm}$; Krecl et al., 2007)—providing an
162 optical depth for all of the particles captured by the filter. The filter punch is then placed in an OCEC
163 analyzer (Sunset instrument, using the EUSAAR_2 protocol) to determine the OC and EC mass,
164 followed by another measurement with the PSAP. The OCEC analysis removes the carbonaceous
165 species and, thus, by comparing the PSAP results obtained before and after the analysis, the relative
166 contribution of the light absorption by EC particles in the total particles optical depth is obtained. The
167 remaining optical depth we attribute as non-EC material. This fraction of the total optical thickness we
168 report as the percentage of the mineral dust absorption on the filter samples (expressed as f_b). For further
169 details concerning the measurements see Svensson et al (2018).

170

171 Some of the filter samples (N=17, **out of 91**) were saturated with too much light absorbing material
172 prohibiting reliable EC measurements despite reducing the sample to a melted equivalent of only 30
173 mL. To mitigate this problem, we calculated the EC indirectly from the analyzed total carbon (TC) for
174 the saturated samples. From OCEC analysis TC is the most robust measured constituent, since it
175 includes both OC and EC and is not affected by their split point, which may be incorrectly placed for
176 very dark filters (Chow et al., 2001). **A slope of 0.099 for the EC:TC ratio for filter samples considered**
177 **non-saturated** ~~A linear relation was fitted for non-saturated filter samples and the obtained correlation~~
178 ~~of $EC = 0.10TC + 0.12$~~ was used to reconstruct the EC content for the filter samples containing high
179 amounts of absorbing particles (see details in supplement and Fig. S33a-b). The slope compares well
180 with the slopes reported for air samples collected at two sites in the Himalayas about 550 km south-east
181 from Sunderdhunga in the Kathmandu valley 32 km (altitude of 2150 m a.s.l.) east of Kathmandu, and
182 Langtang 60 km north of Kathmandu (altitude of 3920 m a.s.l.) (Caricco et al., 2003). There, the authors
183 found that the EC/TC ratio was 0.17 for both sites during the summer monsoon season, but between

184 0.10 and 0.13 during what they described as the ramp-up period and the peak concentration season. The
 185 snow samples do not have an upper limit for particles sizes, whereas the air samples were collected as
 186 PM2.5 (particulate matter collected below an aerodynamic diameter of 2.5 μm). The slopes are rather
 187 similar to our value, and the authors found as well a very strong correlation of 0.89 (r^2) between monthly
 188 average EC and OC.

190 3 Results and discussion

191 3.1 EC deposition in young and old snow samples

192 When the EC content is analyzed from filtered snow samples, a common practice is to convert the
 193 results into mass concentrations [EC], given per volume or mass of melt water (e.g. $\mu\text{g L}^{-1}$ or ng g^{-1}).
 194 A spread in results is often largely due to local processes and specific sampling layer thicknesses. The
 195 mass deposition per unit area \widehat{EC} , on the other hand, can be expected to be less variable with increasing
 196 number of layers used to calculate this value. The deposition in each layer is calculated according to:

$$198 \quad \widehat{EC}_i = [EC]_i \frac{\rho_s}{\rho_w} d_i \quad (1)$$

199
 200 where ρ_s and ρ_w are snow and liquid water densities, respectively. The index i , is the number of the
 201 sampled layer from top to bottom, and $\rho_s/\rho_w d$ is the SWE thickness, d_{SWE} . The \widehat{EC}_i and d_{SWEi} are
 202 transformed to cumulative plots by integrating over the layers from the surface to the bottom. These
 203 profiles are presented in Fig. 2a-f (with each sampling layer represented by a square).

204
 205 The visible snow pit stratigraphy described above in section 2.1 can be observed in the pit profiles. At
 206 the top, the accumulated EC (EC_{acc}) as a function of the accumulated d_{SWE} (SWE_{acc}) portray the
 207 young snow layers, whereas in the bottom of the pits the data points represent the old snow layers (Fig.
 208 2a-f). This pattern (with both young and old snow layers) is visible in pits A, B, C, and D (Fig. 2a-d).
 209 These pits also have the ~~melt~~ enriched LAP layer interleaved between the young and old snow layers,
 210 indicated by the sharp increase (or steep slope) between the young and old snow layers. In the two pits
 211 where this general outline is not visible (pit E Fig. 2e and pit F Fig. 2f), it can be explained by the fact
 212 that pit E extended only to the ~~melt~~ enriched LAP layer (therefore no old snow samples) while pit F had
 213 essentially no young snow samples at the time of sampling (therefore pit F starts with the ~~melt~~ enriched
 214 LAP layer).

215
 216 With the data points for young and old snow appearing rather similar in slope between the pits, the
 217 homogeneity is emphasized further by comparing the observations with common effective constants
 218 for young and old snow (EC_y^* and EC_o^*), respectively. Suitable constants were determined to be close to

219 50 $\mu\text{g m}^{-2}$ per mm SWE for young snow and 150 $\mu\text{g m}^{-2}$ per mm SWE for old snow (see supplement
 220 [section 4](#)). The resulting deposition using EC_y^* and EC_o^* are superimposed over the observations in
 221 Figure 2a-e as dashed lines for young snow and dash-dotted lines for old snow. These lines then
 222 represent the constant deposition of EC as function of accumulated melt water in a column according
 223 to:

$$224 \quad EC_{acc} = constant * SWE_{acc} + offset \quad (2)$$

226 where EC_{acc} is the accumulated EC mass per m^2 and SWE_{acc} is the accumulated melt water in L m^{-2}
 227 (or mm), and the ‘constant’ is the deposition constant. The offsets for young snow are a result of
 228 enhanced observed EC concentration in the top layer, which can numerically be compensated for by
 229 “artificially” adding a small value to (ΔSWE_{acc}) to each pit ([except pit A](#)), which in essence dilute the
 230 top layer, but have marginal effect on the overall picture. This meant simply rewriting the linear relation
 231 above into:

$$232 \quad EC_{acc} = constant * (SWE_{acc} + \Delta SWE_{acc}) \quad (3)$$

233 The ΔSWE_{acc} amounts were chosen by trial and error to be in multiples of 10 mm for simplicity. The
 234 resulting values were 10, 10, 650, 20, and 20 mm for pits [A B](#) through E in order to explain the apparent
 235 offset. A physical interpretation of these numbers may be the loss of water from the surface layer due
 236 to evaporation or sublimation, which enhance $[EC]$ in the top layer. For the old snow layers, snow and
 237 EC were numerically removed in the data by subtracting accumulated EC and SWE (including the ~~melt~~
 238 [enriched LAP](#) layer, when present) down to the old snow layer. This was done such that the first data
 239 point satisfies EC_o^* . Hence, for old snow $[EC]_1 d_{SWE_1} / EC_o^* = SWE_{acc_1}$ where the index (1) represents the
 240 top layer of old snow.

241 By applying the offset values and numerically removing the upper snow layers, we compare the data in
 242 Fig. 2a-f in two separate figures (Fig. 3a-b), one where young snow are grouped together and one for
 243 old snow. In Fig 3a, the observed EC_{acc} is plotted against the EC_{acc} value if EC_y^* is used. In Fig. 3b
 244 the observed EC_{acc} is plotted against the EC_{acc} value if EC_o^* is used. Note that for old snow the first
 245 data point in the different pits will, by definition, be on the 1:1 line. Nevertheless, the consistency
 246 between the pits is striking and the fact that much of the variation in EC_{acc} as function of SWE_{acc} (or
 247 depth in the pit) can be explained by EC_y^* and EC_o^* alone is a very interesting finding.

252 253 ~~Melt~~ [Enriched LAP](#) layer

254 On the contrary to the observed similarities in the different pits between young and old snow, the ~~melt~~
255 **enriched LAP** layer samples do not display similar trends. Instead of being characterized by a common
256 constant, the *EC_{acc}* value as function of *SWE_{acc}* in the ~~melt~~ **enriched LAP** layer differs by orders of
257 magnitude between the different pit profiles. To explore the ~~melt~~ **enriched LAP** layers further, we make
258 use of the constant for young snow, *EC_y^{*}*. Assuming that this is a characteristic value for precipitation
259 during the winter season, we can estimate the required amount of precipitation (*SWE_{acc}*) that is needed
260 to explain the observed *EC_{acc}* deposition. These derived precipitation amounts for each pit are
261 presented in Figure 4 as a function of the relative depth from the surface to the bottom of the pit. Using
262 this approach, pit F corresponds to a total equivalent of about 24200 mm in precipitation, whereas pits
263 B, E, and D represent ~~352800~~, ~~43200~~, and ~~514900~~ mm, respectively. Pits A and C deviate starkly from
264 the others, with ~~376000~~ and ~~554000~~ mm precipitation. Comparing these derived values to other
265 precipitation estimates allows us to provide a temporal perspective required to explain the observed EC
266 in the pits. Other studies have shown that the annual precipitation is very altitude-level dependent in the
267 Himalayas, and based on the altitude of the glaciers alone one would expect less than about 1000 mm
268 in annual precipitation (Anders et al., 2006; Bookhagen and Burbank, 2010). Based on the changes in
269 snow depth, the local precipitation was estimated using the AWS as described in section 2.2. This
270 analysis gave a snow accumulation of about 600 mm SWE in the winter season 2015-2016 and 700 mm
271 in the 2016-2017 winter season at the location of the AWS. Over the season, a fraction of the snow
272 evaporates or sublimates, possibly accounting for a magnitude of mm per day during favorable
273 conditions (Stigter et al., 2018). Further, Mimeau et al. (2019) estimated the sublimation between 12
274 and 15 % of the total annual precipitation in the Khumbu valley, Nepal. This amount might be missed
275 by this method using daily data. Nonetheless, our two precipitation estimates are below the observed
276 annual precipitation of 976 mm in 2012/2013 at 3950 m altitude, about 250 km to the north-west next
277 to the Chhota Shigri glacier front (Azam et al., 2016). Measured with an automatic precipitation gauge
278 (i.e. capturing all precipitation forms), the authors found that the majority of precipitation was during
279 the winter season, and that the summer monsoon contributed with only 12 % to the annual precipitation.
280 Based on these observation estimates, and the similarities with our Sunderdhunga AWS precipitation
281 patterns, we estimate that about 800 ± 200 mm is a characteristic annual precipitation amount close to
282 where the pits were dug. If the precipitation amounts derived to explain the deposited EC in each pit is
283 divided by 800 mm, the minimum number of years required to explain the EC observed in the pit is
284 acquired. With this approach it is clear that it would require decades of precipitation to explain the EC
285 in the ~~melt~~ **enriched LAP** layers in pits A and C. This is unrealistic, especially when the lower levels in
286 pit F from the previous year is compared. Even the difference in EC amount between pits B, E, and D
287 compared to F is much greater than can be explained from aggregating the EC accumulated by one year
288 of precipitation in a single melt layer. **At the same time, the dry deposition of EC probably accounts for**
289 **only a few percent of the deposition. With a dry deposition velocity of EC of 0.3 mm/s (Emerson et al.,**

290 2018) and an atmospheric concentration of $0.3 \mu\text{g m}^{-3}$, reported at similar altitude at the Nepal Pyramid
291 station during the pre-monsoon (Bonasoni et al., 2010), the dry deposition can be estimated to $2800 \mu\text{g}$
292 m^{-2} annually, which several orders of magnitude lower than what is encountered in the enriched LAP
293 layers. Thus, this leads us to propose that EC must have been transported laterally in the surface layer
294 during the melt period in the summer of 2016 and converged in the altitude range where the pits were
295 dug. From Figure 1 it can be seen that the pits were dug in a complex terrain where slopes with
296 increasing gradient are reaching up to the summit towards the southwest.

297

298 The data and analysis presented above lead us to propose that the old snow layers observed in pit F
299 from 2015 are the same old snow layers observed for the pits dug in 2016. The EC equivalent
300 precipitation profile of pit F presented in Figure 4 suggests that strong melting had taken place already
301 in summer 2015. Hence, the old snow is composed of snow from at least the season 2013-2014 (or
302 perhaps also earlier seasons). Stratigraphy analysis for pit F presented in Svensson et al. (2018)
303 suggested that the snow deposition represented five seasons. The amount of precipitation represented
304 by the EC deposition (cf. Figure 4) in the old snow is about 24200 mm , which suggests that the EC was
305 deposited over several seasons, but less than 5 seasons. Another strong melt took place in 2016, possibly
306 leading to melting all of the snow from the season 2015-2016. In addition, during the melting phase,
307 water and snow particulates could be transported down the slopes from areas of the glacier with steep
308 slopes. Because the steepness of the slope decreases towards the valley, this resulted in a convergence
309 of percolated material from areas above the sampling sites. The young snow is likely part of the 2016-
310 2017 winter season that had started to accumulate before the sampling in October 2016 was
311 commenced. This is confirmed by AWS data that indicates intermittent snow events in October 2016.
312 At the AWS location a seasonal snow cover was in place in December 2016.

313

314 3.3 Mineral dust fraction in snow

315 An initial inspection of the mineral fractional absorption on the filters did not reveal any special
316 common pattern in concentration between the different pits, except for the melt enriched LAP layer
317 samples, which appeared to have higher concentrations than the other samples. In Figure 5, the data is
318 grouped according to the pit stratigraphy classification, and although the absolute range of MD fractions
319 in young snow samples is very large (5 to 71 %), the quartile range is only between 32 to 48 % with a
320 median value of 39 %. The median value for old snow is somewhat larger at 46 %, along with the range
321 and quartiles, which are closer together, from 26 to 70 % and from 43 to 50 %, respectively. The range
322 of values for the melt enriched LAP layer are consistently higher compared to the other two snow types.
323 The median is 78 % with a range and quartiles of 48 to 95 % and 74 to 82 %, respectively. Note that
324 from a total of 95 samples only 16 are from the melt LAP layer. As with EC, MD has the propensity to
325 remain at the snow surface with melting (e.g. Doherty et al., 2013).

326
327
328
329
330
331
332
333
334
335
336
337
338
339
340
341
342
343
344
345
346
347
348
349
350
351
352
353
354
355
356
357
358
359
360
361

Due to the typically heavy loading of material on the filters obtained in the ~~melt~~ enriched LAP layer, those values should be taken with caution, **however**. Non-linear effects could skew the resulting light absorption fractions towards larger values ~~science~~ **since** with a very heavy loading (dark filter) the contribution by remaining particles may be over-estimated. This is because the relative contribution by additional light absorbing material decreases as the amount of material increases on very dark filters. In an extreme case, black on black will not add any contribution. The larger range of values in young snow compared to old snow is possibly an effect from the geometric thickness of the sampled slabs, which are in young snow generally thinner than in old snow, and that the density of young snow is typically less than the density of old snow. This results in each of the sampled segments in young snow representing less deposition of both water and LAP and, therefore, presenting a larger variability. Nevertheless, the ensemble of data presents similar median values for both young and old snow. The median of the percentage of the mineral dust absorption f_D value for young and old snow samples together becomes 44 %. The specific absorption by minerals is expected to be orders of magnitude smaller than BC (e.g. Utry et al., 2015), and the same is expected with respect to EC. This suggests that the deposition of minerals in the snow is orders of magnitude larger than EC. If we simply scale our characteristic EC constants (EC_y^* and EC_o^*), with the median of f_D and the ratio between their specific mass absorption coefficients (MAC), according to:

$$\frac{f_D}{(1-f_D)} \frac{MAC_{EC}}{MAC_D} EC_c = D_c \quad (4)$$

we arrive at a mass concentration for minerals. We use a MAC for BC of $7.5 \text{ m}^2 \text{ g}^{-1}$ (Bond and Bergstrom, 2006). The MAC for the minerals is not known and can vary significantly, but for the sake of this test we use a MAC value representative for the mineral quartz with $0.0023 \text{ m}^2 \text{ g}^{-1}$ (Utry et al., 2015). If we use these values we arrive at a range of $128\text{-}384 \text{ } \mu\text{g g}^{-1}$ of minerals in the snow. This is in range with previous gravimetric observations from Himalaya (e.g. Thind et al., 2019; Zhang et al., 2018).

3.4 Discussion

Our results indicate that the contribution to light absorption by minerals can be comparable to light absorption by EC in the Sunderdhunga area at about 5 km altitude. This translates into a mass concentration ratio between EC and minerals of more than three orders of magnitude. These large ratios are typically not reported for air samples because much of the deposited minerals are likely from local sources. This supports a hypothesis of a positive climate feedback that results in a reduction of snow cover and the exposure to larger sources of minerals.

362 For the Tibetan plateau, Zhang et al. (2018) estimated that the retreat of the snow cover could be
363 advanced by more than a week due to LAP in snow. In their estimates, BC accounted for most of this
364 effect and dust advanced the melting by about one day. The BC concentration in snow used in their
365 calculations were about one order of magnitude larger than our derived values from the profiles in the
366 snow pits. This difference can be attributed to the significant contribution of aerosol particle dry
367 deposition in arid regions (Wang et al., 2014), but the range of values presented in their Table 2 reveals
368 a potential problem from sampling surface snow. Post depositional processes (e.g.
369 sublimation/evaporation, hoar formation, snow drift) can alter the concentration at a given location
370 relatively fast, which is less of a problem if a deeper layer of the snow pack is investigated instead of
371 solely the surface snow. Simply taking a larger vertical slab is not sufficient as is evident from the melt
372 layer in the present study. The ~~melt~~ enriched LAP layer in the pits can be studied to characterize the
373 short-term seasonal surface albedo, but the aerosol concentrations cannot be directly related to the
374 deposition. The consistency between pits and different sampling seasons in the integrated deposition
375 profiles above and below the ~~melt~~ enriched LAP layer show the strength in the data collected from snow
376 pits in comparison to snap-shot conditions of surface snow.

377

378 4 Conclusions

379 In this study we aimed at characterizing the observed deposition of EC in the glacier snow in the
380 Sunderdhunga valley and to estimate the contribution from minerals to LAP in the snow. The analysis
381 illustrates that in the sampling area of Durga Kot and Bhanolti glaciers, the deposition of EC in young
382 snow (from current winter season) is characterized by approximately $50 \mu\text{g m}^{-2} \text{mm}^{-1}$ SWE water, which
383 is in the range of other observations. The median fraction of light absorption caused by minerals was
384 about 39 % (Q1=32, Q3=48). In old snow (from previous winter seasons), the deposition was
385 characterized by about $150 \mu\text{g m}^{-2} \text{mm}^{-1}$ SWE water. The reason for this difference can simply be due
386 to a larger deposition in the years before sampling was conducted, or that more water had the chance to
387 leave the snow-pack of older snow. Different from young snow, old snow have had to survive at least
388 one summer season. The median fraction of light absorption was 46 % (Q1=43, Q3=50) by minerals in
389 the old snow layer. Although the variability within each layer is rather large, the obtained lower median
390 fraction for young snow is consistent with the fact that old snow is more exposed to rock surfaces free
391 of snow during the summer season.

392

393 Between these two layers of old and young snow, a clearly visible and very dark layer was present. This
394 layer was most likely a result of strong melting that took place in the summers of 2015 and 2016 as
395 discussed in 3.2. However, the high concentration of EC found in this layer cannot simply be explained
396 by a collapse of the snow-pack vertically, and thus it is concluded that lateral transport of LAP
397 (including EC and minerals) took place that resulted in a convergence of material in the altitude range

398 of the snow pits. Different from the other two layers (young and old snow), this ~~melt~~ enriched LAP
399 layer presented large differences with respect to EC content among the different pits. The fraction of
400 light absorption by minerals was the highest of the three layers and was about 80 % (Q1=74, Q3=82).

401

402 The profiles of EC and the mineral absorption fraction show good agreement between subsequent years
403 and among different pits. At the same time, the topography in this mountainous region of Himalaya
404 evidently causes great complexity with respect to the distribution of LAP in the snow surface layer
405 during periods of strong melt. Although data is limited in spatial and temporal dimensions our results
406 are useful for large scale radiation impact assessments of EC deposition and minerals. In small scale
407 regional studies, however, the effects of complex topography and spatial variability should be
408 considered separately. Future work should further study the mineral dust and its composition in the
409 area, in order to more accurately elucidate dust role in the snow radiation ~~scheme~~ state in this part of
410 the Himalaya.

411

412 Data availability

413 All data are available upon request.

414

415 Author contributions

416 J. Sv, H.H, E.A., N.D., H.L., participated in the field expedition. S.T., R.H., V.S., M. L., H.L., A.H.
417 handled project administration. Data analysis was performed by J. Sv. and J. St. Funding acquisition:
418 A.H. Supervision M.L. and H.L. J. Sv led the writing of the manuscript with J. St., with input from all
419 other co-authors.

420

421 Completing interests.

422 The authors declare that they have no conflict of interest.

423

424 Acknowledgements

425 This work has been supported by the Academy of Finland project: Absorbing Aerosols and Fate of
426 Indian Glaciers (AAFIG; project number 268004), and the Academy of Finland consortium: “Novel
427 Assessment of Black Carbon in the Eurasian Arctic: From Historical Concentrations and Sources to
428 Future Climate Impacts” (NABCEA project number 296302). J.Svensson acknowledges support from
429 the two Finnish foundations: Maj and Tor Nessling and Oskar Huttunen; as well as the invited scientist
430 grant from the UGA. J. Ström is part of the Bolin Centre for Climate Research, and acknowledges the
431 Swedish Research Council grant 2017-03758. We are thankful for Daniela Tuomala’s work with the
432 filter analyzes, as well as the strenuous assistance given by Sherpas and mountain guides during the
433 expeditions to the Sunderdhunga valley.

434 **References**

- 435 Anders, A. M., Roe, G. H., Hallet, B., Montgomery, D. R., Finnegan, N. J., and Putkonen, J.: Spatial
436 patterns of precipitation and topography in the Himalaya, *Geol. Soc. Am. Special Papers*, 398, 39–53,
437 2006.
- 438 Azam, M. F., Ramanathan, A. L., Wagnon, P., Vincent, C., Linda, A., Berthier, E., Sharma, P., Mandal,
439 A., Angchuk, T., Singh, V. B., and Pottakkal, J. G.: Meteorological conditions, seasonal and annual
440 mass balances of Chhota Shigri Glacier, western Himalaya, India, *Ann. Glaciol.*, 57, 328–338, doi:
441 10.3189/2016AoG71A570, 2016.
- 442 Bond, T. C., and Bergstrom, R. W.: Light absorption by carbonaceous particles: An investigative
443 review, *Aerosol Sci. Tech.*, 40, 27–67, doi:10.1080/02786820500421521, 2006.
- 444 Bonasoni, P., Laj, P., Marinoni, A., Sprenger, M., Angelini, F., Arduini, J., Bonafè, U., Calzolari, F.,
445 Colombo, T., Decesari, S., Di Biagio, C., di Sarra, A. G., Evangelisti, F., Duchi, R., Facchini, MC.,
446 Fuzzi, S., Gobbi, G. P., Maione, M., Panday, A., Roccatò, F., Sellegri, K., Venzac, H., Verza, G. P.,
447 Villani, P., Vuillermoz, E., and Cristofanelli, P.: Atmospheric Brown Clouds in the Himalayas: first
448 two years of continuous observations at the Nepal Climate Observatory-Pyramid (5079 m), *Atmos.*
449 *Chem. Phys.*, 10, 7515–7531, doi:10.5194/acp-10-7515-2010, 2010.
- 450 Bookhagen, B. and Burbank, D. W.: Toward a complete Himalayan hydrological budget:
451 Spatiotemporal distribution of snowmelt and rainfall and their impact on river discharge, *J. Geophys.*
452 *Res.*, 115, F03019, doi:10.1029/2009JF001426, 2010.
- 453 Carrico, C. M., Bergin, M. H., Shrestha, A., Dibb, J. E., Gomes, L., and Harris, J.M.: The importance
454 of carbon and mineral dust to seasonal aerosol properties in the Nepal Himalayas, *Atmos. Environ.*, 37,
455 2811–2824, 2003.
- 456 Chow, J. C., Watson, J. G., Crow, S., Lowenthal, D. H., and Merrifield, T.: Comparison of IMPROVE
457 and NIOSH carbon measurements, *Aerosol Sci. Tech.*, 34, 23–34, 2001.
- 458 Doherty, S. J., Grenfell, T. C., Forsström, S., Hegg, D. L., Brandt, R. E., and Warren, S. G.: Observed
459 vertical redistribution of black carbon and other insoluble light-absorbing particles in melting snow, *J.*
460 *Geophys. Res.-Atmos.*, 118, 5553–5569, doi.org/10.1002/jgrd.50235, 2013.
- 461 Emerson, E. W., Katich, J. M., Schwarz, J. P., McMeeking, G. R., and Farmer, D. K.: Direct
462 Measurements of Dry and Wet Deposition of Black Carbon Over a Grassland, *J. Geophys. Res.-Atmos.*,
463 123, 12277–212290, doi.org/10.1029/2018JD028954, 2018.
- 464 Flanner, M. G., Zender, C. S., Randerson, J. T., and Rasch, P. J.: Present-day climate forcing and
465 response from black carbon in snow, *J. Geophys. Res.-Atmos.*, 112, D11202,
466 doi.org/10.1029/2006JD008003, 2007.
- 467 Gertler, C. G., Puppala, S. P., Panday, A., Stumm, D., and Shea, J.: Black carbon and the Himalayan
468 cryosphere: A review, *Atmos. Environ.*, 125, 404–417, doi.org/10.1016/j.atmosenv.2015.08.078, 2016.
- 469 He, C., Flanner, M. G., Chen, F., Barlage, M., Liou, K.-N., Kang, S., Ming, J., and Qian, Y.: Black
470 carbon-induced snow albedo reduction over the Tibetan Plateau: uncertainties from snow grain shape
471 and aerosol–snow mixing state based on an updated SNICAR model, *Atmos. Chem. Phys.*, 18, 11507–
472 11527, doi.org/10.5194/acp-18-11507-2018, 2018.
- 473 Helfricht, K., Hartl, L., Koch, R., Marty, C., and Olfes, M.: Obtaining sub-daily new snow density from
474 automated measurements in high mountain regions, *Hydrol. Earth Syst. Sci.*, 22, 2655–2668,
475 doi.org/10.5194/hess-22-2655-2018, 2018.

476 Hooda, R.K., Kivekäs, N., O'Connor, E.J., Collaud Coen, M., Pietikäinen, J.P., Vakkari, V., Backman,
477 J., Henriksson, S.V., Asmi, E., Komppula, M., Korhonen, H., Hyvärinen, A. P., Lihavainen, H.: Driving
478 factors of aerosol properties over the foothills of central Himalayas based on 8.5 Years continuous
479 measurements, *J. Geophys. Res. Atmos.*, 123, doi.org/10.1029/2018JD029744, 421-13,442, 2018.

480 Jacobi, H.-W., Lim, S., Ménégoz, M., Ginot, P., Laj, P., Bonasoni, P., Stocchi, P., Marinoni, A., and
481 Arnaud, Y.: Black carbon in snow in the upper Himalayan Khumbu Valley, Nepal: observations and
482 modeling of the impact on snow albedo, melting, and radiative forcing, *The Cryosphere*, 9, 1685–1699,
483 doi.org/10.5194/tc-9-1685-2015, 2015.

484 Jacobson, M. Z.: Climate response of fossil fuel and biofuel soot, accounting for soot's feedback
485 to snow and sea ice albedo and emissivity, *J. Geophys. Res.-Atmos.*, 109, D21201,
486 doi.org/10.1029/2004jd004945, 2004.

487 Kaspari, S., Painter, T. H., Gysel, M., Skiles, S. M., and Schwikowski, M.: Seasonal and elevational
488 variations of black carbon and dust in snow and ice in the Solu-Khumbu, Nepal and estimated radiative
489 forcings, *Atmos. Chem. Phys.*, 14, 8089–8103, doi.org/10.5194/acp-14-8089-2014, 2014.

490 Krecl, P., Ström, J., and Johansson, C.: Carbon content of atmospheric aerosols in a residential area
491 during the wood combustion season in Sweden, *Atmos. Environ.*, 41, 6974–6985,
492 doi.org/10.1016/j.atmosenv.2007.06.025, 2007.

493 Kopacz, M., Mauzerall, D. L., Wang, J., Leibensperger, E. M., Henze, D. K., and Singh, K.: Origin and
494 radiative forcing of black carbon transported to the Himalayas and Tibetan Plateau, *Atmos. Chem.
495 Phys.*, 11, 2837–2852, doi.org/10.5194/acp-11-2837-2011, 2011.

496 Li, C., Bosch, C., Kang, S., Andersson, A., Chen, P., Zhang, Q., Cong, Z., Chen, B., Qin, D., and
497 Gustafsson, O.: Sources of black carbon to the Himalayan-Tibetan Plateau glaciers, *Nature Commun.*,
498 7, 12574, doi.org/10.1038/ncomms12574, 2016.

499 Ménégoz, M., Krinner, G., Balkanski, Y., Boucher, O., Cozic, A., Lim, S., Ginot, P., Laj, P., Gallée,
500 H., Wagnon, P., Marinoni, A., and Jacobi, H. W.: Snow cover sensitivity to black carbon deposition in
501 the Himalayas: from atmospheric and ice core measurements to regional climate simulations, *Atmos.
502 Chem. Phys.*, 14, 4237–4249, doi.org/10.5194/acp-14-4237-2014, 2014.

503 Mimeau, L., Esteves, M., Zin, I., Jacobi, H.-W., Brun, F., Wagnon, P., Koirala, D., and Arnaud, Y.:
504 Quantification of different flow components in a high-altitude glacierized catchment (Dudh Koshi,
505 Himalaya): some cryospheric-related issues, *Hydrol. Earth Syst. Sci.*, 23, 3969–3996,
506 doi.org/10.5194/hess-23-3969-2019, 2019.

507 Ming, J., Du, Z., Xiao, C., Xu, X., and Zhang, D.: Darkening of the mid-Himalaya glaciers since 2000
508 and the potential causes, *Environ. Res. Lett.*, 7, 014021, doi:10.1088/1748-25 9326/7/1/014021, 2012.

509 Ming, J., Xiao, C., Du, Z., and Yang, X.: An Overview of Black Carbon Deposition in High Asia
510 Glaciers and its Impacts on Radiation Balance, *Adv. Water Resour.*, 55, 80–87, 2013.

511 Petzold, A., Ogren, J. A., Fiebig, M., Laj, P., Li, S.-M., Baltensperger, U., Holzer-Popp, T., Kinne, S.,
512 Pappalardo, G., Sugimoto, N., Wehrli, C., Wiedensohler, A., and Zhang, X.-Y.: Recommendations for
513 reporting "black carbon" measurements, *Atmos. Chem. Phys.*, 13, 8365–8379, doi.org/10.5194/acp-13-
514 8365-2013, 2013.

515 Raatikainen, T., Hyvärinen, A. P., Hatakka, J., Panwar, T. S., Hooda, R. K., Sharma, V. P., and
516 Lihavainen, H.: The effect of boundary layer dynamics on aerosol properties at the Indo-Gangetic plains
517 and at the foothills of the Himalayas, *Atmos. Environ.*, 89, 548– 555,
518 doi.org/10.1016/j.atmosenv.2014.02.058, 2014.

519 Ramanathan, V. and Carmichael, G.: Global and regional climate changes due to black carbon, *Nat.*
520 *Geosci.*, 1, 221–227, doi.org/10.1038/ngeo156, 2008.

521 Santra, S., Verma, S., Fujita, K., Chakraborty, I., Boucher, O., Takemura, T., Burkhart, J. F., Matt, F.,
522 and Sharma, M.: Simulations of black carbon (BC) aerosol impact over Hindu Kush Himalayan sites:
523 validation, sources, and implications on glacier runoff, *Atmos. Chem. Phys.*, 19, 2441–2460,
524 doi.org/10.5194/acp-19-2441-2019, 2019.

525 Sarangi, C., Qian, Y., Rittger, K., Bormann, K. J., Liu, Y., Wang, H., Wan, H., Lin, G., and Painter, T.
526 H.: Impact of light-absorbing particles on snow albedo darkening and associated radiative forcing over
527 high-mountain Asia: high-resolution WRF-Chem modeling and new satellite observations, *Atmos.*
528 *Chem. Phys.*, 19, 7105–7128, doi.org/10.5194/acp-19-7105-2019, 2019.

529 Skiles, S. M., Flanner, M., Cook, J. M., Dumont, M., and Painter, T. H.: Radiative forcing by light-
530 absorbing particles in snow, *Nat. Clim. Change*, 8, 964–971, doi.org/10.1038/s41558-018-0296-5,
531 2018.

532 Stigter, E. E., Maxime Litt, A., Jakob Steiner, F., Pleun Bonekamp, N. J., Joseph Shea, M., and
533 Immerzeel, W. W.: The importance of snow sublimation on a himalayan glacier. *Front. Earth Sci.* 6:108,
534 doi: 10.3389/feart.2018.00108, 2018.

535 Svensson, J., Ström, J., Kivekäs, N., Dkhar, N. B., Tayal, S., Sharma, V. P., Jutila, A., Backman, J.,
536 Virkkula, A., Ruppel, M., Hyvärinen, A., Kontu, A., Hannula, H.-R., Leppäranta, M., Hooda, R. K.,
537 Korhola, A., Asmi, E., and Lihavainen, H.: Light-absorption of dust and elemental carbon in snow in
538 the Indian Himalayas and the Finnish Arctic, *Atmos. Meas. Tech.*, 11, 1403–1416,
539 doi.org/10.5194/amt-11-1403-2018, 2018.

540 Thind, P. S., Chandel, K. K., Sharma, S. K., Mandal, T. K., and John, S.: Light-absorbing impurities in
541 snow of the Indian Western Himalayas: impact on snow albedo, radiative forcing, and enhanced
542 melting, *Environ. Sci. Pollut. Res. Int.*, 26, 7566–7578, doi.org/10.1007/s11356-019-04183-5, 2019.

543 Utry, N., Ajtai, T., Pintér, M., Tombácz, E., Illés, E., Bozóki, Z., and Szabó, G.: Mass-specific optical
544 absorption coefficients and imaginary part of the complex refractive indices of mineral dust components
545 measured by a multi-wavelength photoacoustic spectrometer, *Atmos. Meas. Tech.*, 8, 401–410,
546 doi.org/10.5194/amt-8-401-2015, 2015.

547 Wang, Z. W., Gallet, J. C., Pedersen, C. A., Zhang, X. S., Ström, J., and Ci, Z. J.: Elemental carbon in
548 snow at Changbai Mountain, northeastern China: concentrations, scavenging ratios, and dry deposition
549 velocities, *Atmos. Chem. Phys.*, 14, 629–640, doi.org/10.5194/acp-14-629-2014, 2014.

550 Warren, S. and Wiscombe, W.: A model for the spectral albedo of snow II. Snow containing
551 atmospheric aerosols, *J. Atmos. Sci.*, 37, 2734–2745, 1980.

552 Xu, B., Cao, J., Hansen, J., Yao, T., Joswiak, D.R., Wang, N., Wu, G., Wang, M., Zhao, H., Yang, W.,
553 Liu, X., and He, J.: Black soot and the survival of Tibetan glaciers, *P. Natl. Acad. Sci. USA*, 106,
554 22114–22118, doi.org/10.1073/pnas.0910444106, 2009.

555 Zhang, R., Wang, H., Qian, Y., Rasch, P. J., Easter, R. C., Ma, P.-L., Singh, B., Huang, J., and Fu, Q.:
556 Quantifying sources, transport, deposition, and radiative forcing of black carbon over the Himalayas
557 and Tibetan Plateau, *Atmos. Chem. Phys.*, 15, 6205–6223, doi.org/10.5194/acp-15-6205-2015, 2015.

558 Zhang, Y., Kang, S., Sprenger, M., Cong, Z., Gao, T., Li, C., Tao, S., Li, X., Zhong, X., Xu, M., Meng,
559 W., Neupane, B., Qin, X., and Sillanpää, M.: Black carbon and mineral dust in snow cover on the
560 Tibetan Plateau, *The Cryosphere*, 12, 413–431, doi.org/10.5194/tc-12-413-2018, 2018.

561 Table 1. Snow pit details from Sunderdhunga valley. Durga Kot glacier snow pits are A-B, while C-F are from Bhanolti glacier.

562

Snow pit ID and elevation (m a.s.l)	Depth interval (cm)	Snow density (g cm ⁻³)		Water equivalent (mm m ⁻²)	TC analyzed (μg L ⁻¹)	EC (μg L ⁻¹)		EC deposition (μg m ⁻²)	fD (%)
		Measured	Assumed			Analyzed	Reconstructed		
A, 5055	0-3	0.38		11.4	1130	-	120	1364	24.6
	3-6	0.38		11.4	238	18	-	207	29.2
	6-9	0.35		10.5	477	47	-	495	40.4
	9-12	0.37		11.1	30300	-	3125	34688	-
	12-15	0.39		11.7	1307404	-	134685	1575819	76.1
	15-20		0.50	25.0	68177	-	7034	175855	55.1
	20-25		0.50	25.0	1398	278	-	6945	47.9
	25-30		0.50	25.0	1549	147	-	3684	49.8
	30-35		0.50	25.0	1769	271	-	6787	41.9
	35-40		0.50	25.0	1466	251	-	6273	46.5
	40-45		0.50	25.0	883	141	-	3528	44.6
	45-50		0.50	25.0	751	142	-	3553	43.1
	50-60		0.50	50.0	1090	171	-	8544	51.5
	60-70		0.50	50.0	763	88	-	4412	45.9
B, 5055	0-3	0.40		12.0	1542	95	-	1143	38.3
	3-6	0.40		12.0	693	30	-	364	27.5
	6-9	0.39		11.6	31710	-	3291	38015	77.8
	9-12	0.33		9.9	69667	-	7210	71378	75.0
	12-15	0.33		9.9	3498	-	374	3699	50.6
	15-19		0.50	20.0	-	-	267	5348	49.9
	19-29		0.50	50.0	1534	246	-	12319	49.8
	29-39		0.50	50.0	1295	190	-	9480	46.2
	39-49		0.50	50.0	1517	248	-	12407	52.1

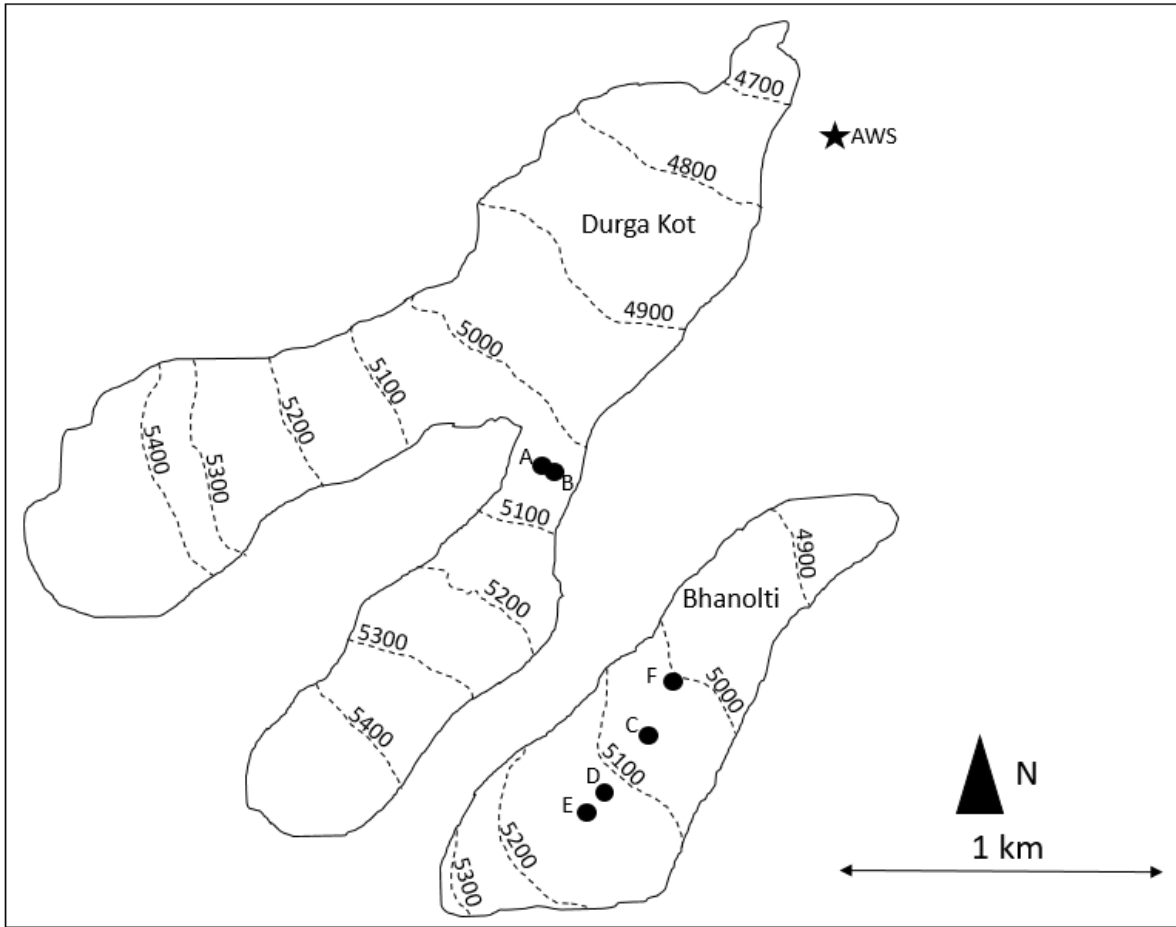
	49-59		0.50	50.0	1753	182	-	9100	40.2
	59-69		0.50	50.0	733	103	-	5156	41.2
	69-79		0.50	50.0	730	102	-	5121	44.9
C, 5068	0-3	0.40		12.0	2386	-	249	2983	47.6
	3-6	0.39		11.7	590	45	-	523	31.6
	6-11	0.39		19.5	372	34	-	658	59.4
	11-16	0.42		21.0	799	93	-	1959	54.8
	16-21	0.46		23.0	1074	141	-	3240	58.0
	21-26		0.50	25.0	1047065	-	107865	2696629	-
	26-31		0.50	25.0	4480	370	-	9257	62.0
	31-36		0.50	25.0	684	80	-	1988	58.9
	36-41		0.50	25.0	906	150	-	3746	43.6
	41-46		0.50	25.0	658	126	-	3159	44.2
	46-56		0.50	50.0	863	137	-	6871	43.5
	56-66		0.50	50.0	1191	156	-	7803	45.7
	66-76		0.50	50.0	832	144	-	7222	44.9
	76-86		0.50	50.0	802	94	-	4709	45.9
	86-96		0.50	50.0	416	51	-	2543	42.6
	96-106		0.50	50.0	609	78	-	3913	45.3
	106-116		0.50	50.0	692	76	-	3821	50.0
	116-126		0.50	50.0	500	46	-	2322	57.9
	126-136		0.50	50.0	1265	108	-	5386	59.0
D, 5125	0-3	0.39		11.7	1135	127	-	1487	35.2
	3-6	0.39		11.7	1012	91	-	1068	34.0
	6-9	0.37		11.1	449	30	-	337	42.6
	9-12	0.37		11.1	810	41	-	450	47.3
	12-15	0.37		11.0	1089	84	-	916	48.5
	15-18	0.37		11.0	357	32	-	353	38.6
	18-21	0.36		10.8	918	59	-	637	38.5
	21-24	0.42		12.6	274		36	448	70.8
	24-27	0.42		12.6	322	23	-	293	57.2

	27-30	0.36		10.8	443	28	-	297	36.3
	33-36	0.36		10.8	2393		253	2734	95.1
	36-39	0.45		13.5	1714		186	2506	77.6
	39-42	0.45		13.5	6806		710	9591	77.1
	42-44		0.50	10.0	177424		18313	183125	-
	44-49		0.50	20.0	9733		1025	20504	60.1
	49-54		0.50	25.0	5708	665	-	16635	59.5
	54-59		0.50	25.0	1743	232	-	5798	69.6
	59-69		0.50	50.0	901	129	-	6459	46.1
E, 5143	0-3	0.33		9.9	992	128	-	1268	35.9
	3-6	0.33		9.9	422	63	-	622	41.4
	6-9	0.37		11.1	891	81	-	903	25.9
	9-12	0.31		9.3	569	41	-	380	43.0
	12-15	0.31		9.3	806	73	-	681	27.7
	15-18	0.29		8.7	750	35	-	302	41.0
	18-21	0.29		8.7	345	22	-	193	55.6
	21-24	0.39		11.7	644		81	943	4.5
	24-27	0.38		11.4	500	50	-	566	27.0
	27-30	0.38		11.4	439	65	-	739	56.7
	30-33	0.40		12.0	395	53	-	635	49.4
	33-36	0.40		12.0	642	26	-	308	27.3
	36-39	0.44		13.2	397	33	-	430	38.9
	39-42	0.44		13.2	1250	53	-	705	34.8
	42-45	0.44		13.2	1148	75	-	988	48.4
	45-48	0.45		13.5	828	169	-	2287	81.1
	48-51	0.45		13.5	901	131	-	1775	77.7
	51-54	0.45		13.5	617	58	-	786	85.8
	54-55	0.45		4.5	-	-	4694	21125	85.8
	55-60		0.50	25.0	69606	-	7198	179946	85.8
F, 5008	0-3		0.35	10.5	4075	66		690	77.9
	3-6		0.40	12.0	4821	273		3271	60.8

6-10	0.40	16.0	17686		1828	29242	69.5
10-15	0.50	25.0	3555	233		5830	60.3
15-20	0.50	25.0	859	111		2786	33.1
20-30	0.50	50.0	1324	141		7036	49.2
30-40	0.50	50.0	807	106		5278	39.6
40-50	0.50	50.0	890	98		4907	36.7
50-60	0.50	50.0	2825	270		13484	49.5
60-70	0.50	50.0	1228	179		8965	39.9
70-80	0.50	50.0	696	93		4650	36.1
80-90	0.50	50.0	483	73		3640	35.8
90-100	0.50	50.0	1190	144		7190	43.9
100-110	0.50	50.0	652	79		3965	29.5
110-120	0.50	50.0	554	57		2846	25.7

563

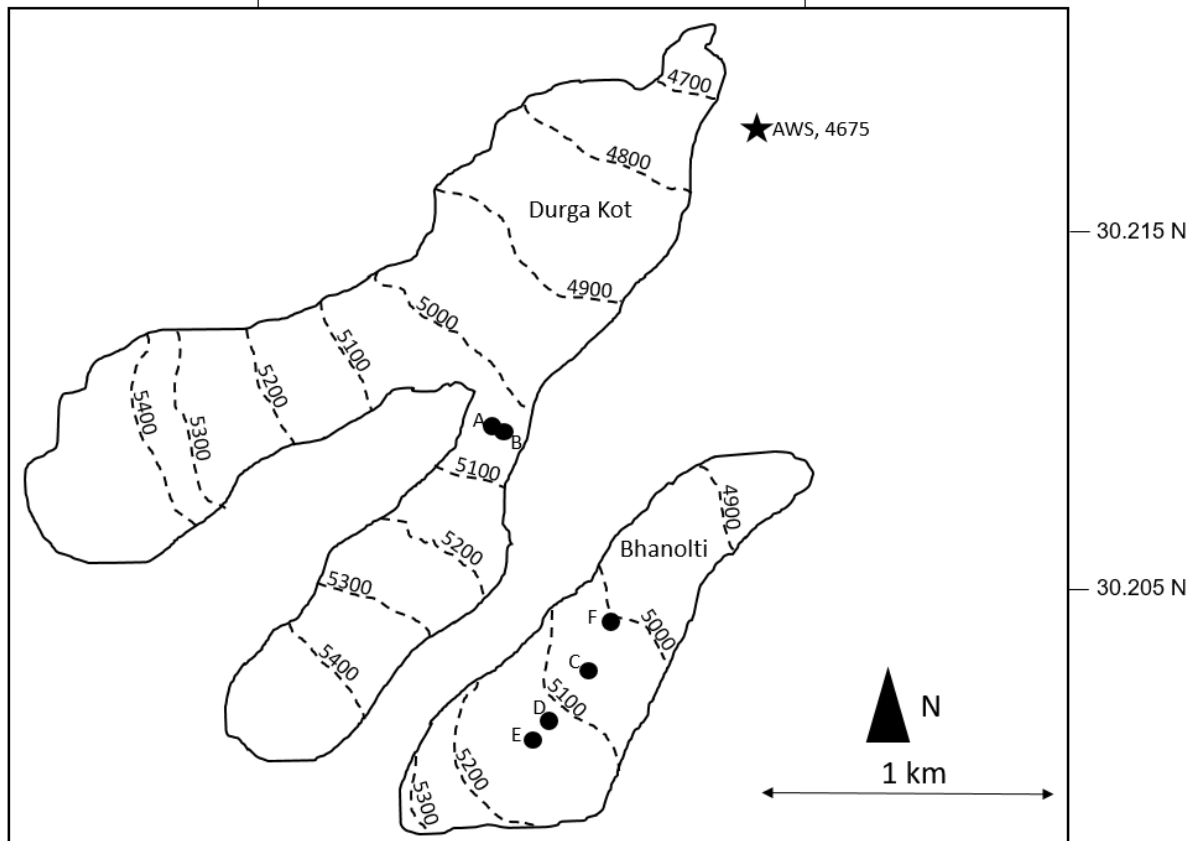
564



565

79.845 E

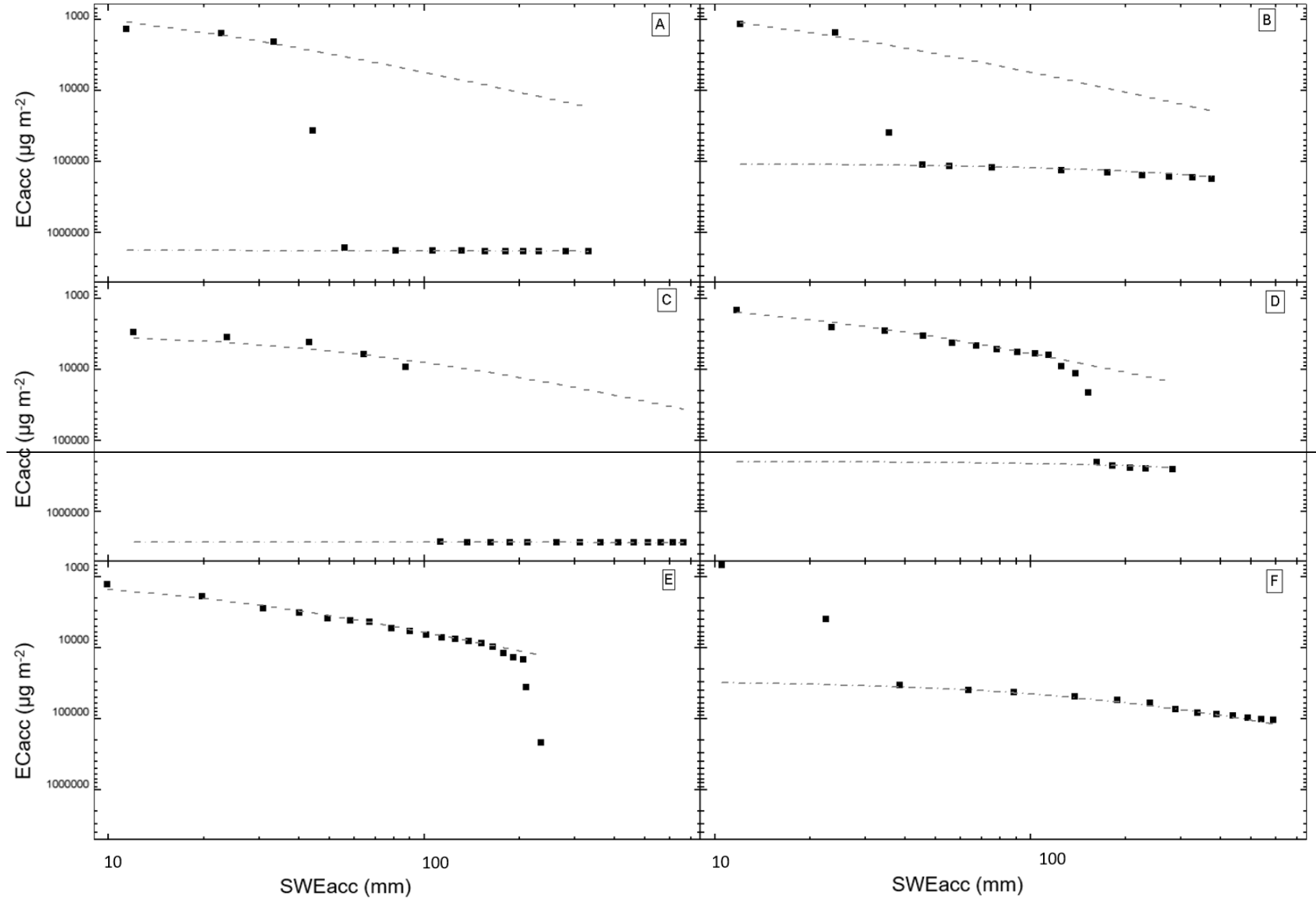
79.860 E

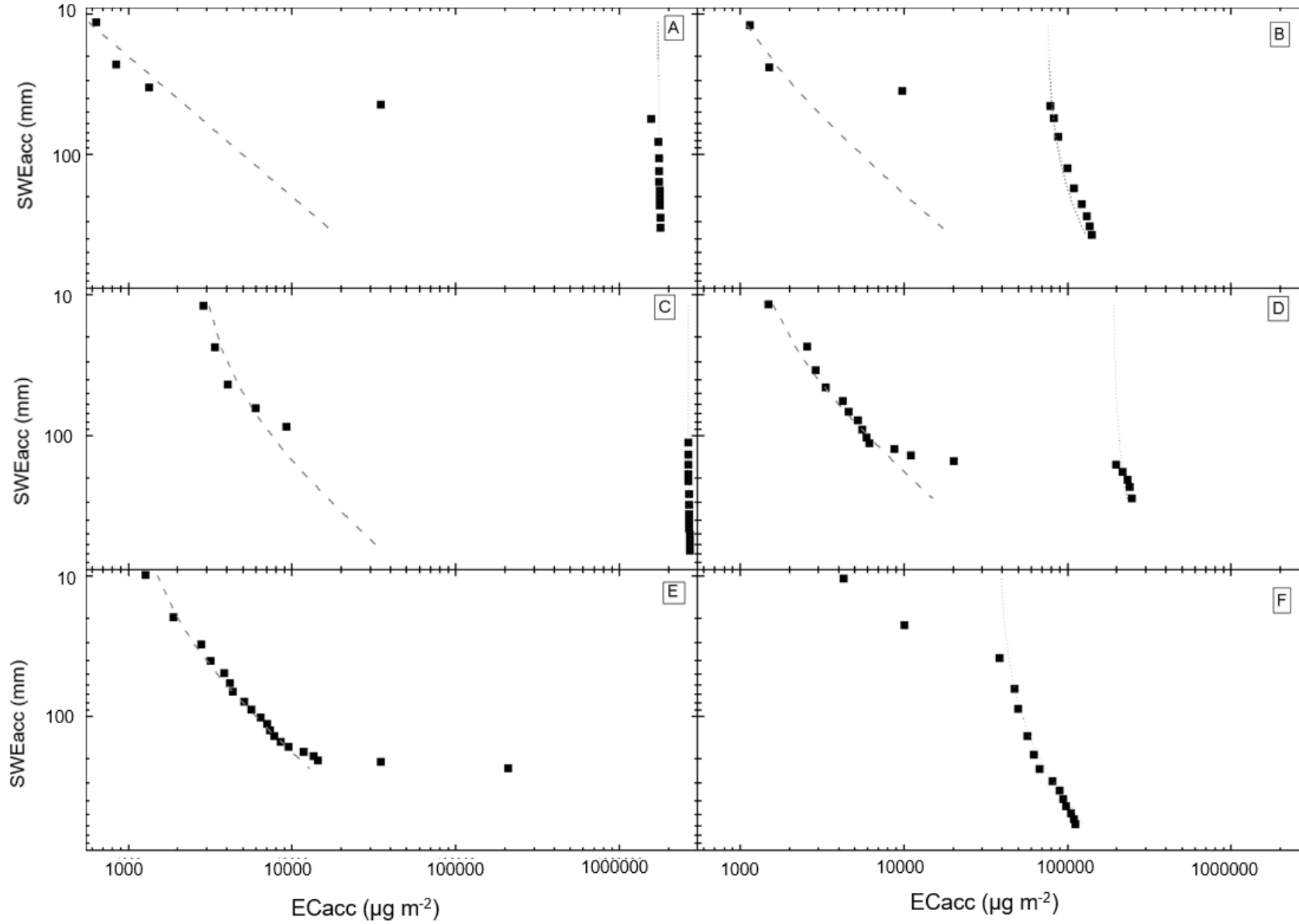


566

567

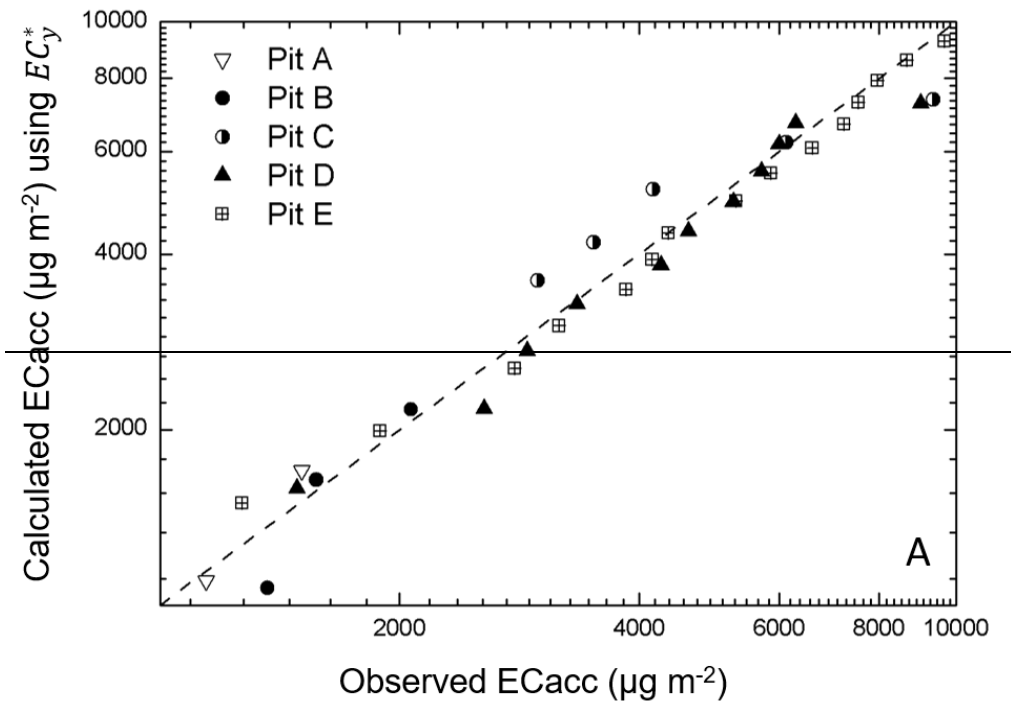
568 Figure 1. Map of glaciers with the location of the snow pits (black dots) and AWS indicated **with a star**.
569 **Dashed lines on the glacier refer to iso-lines** .



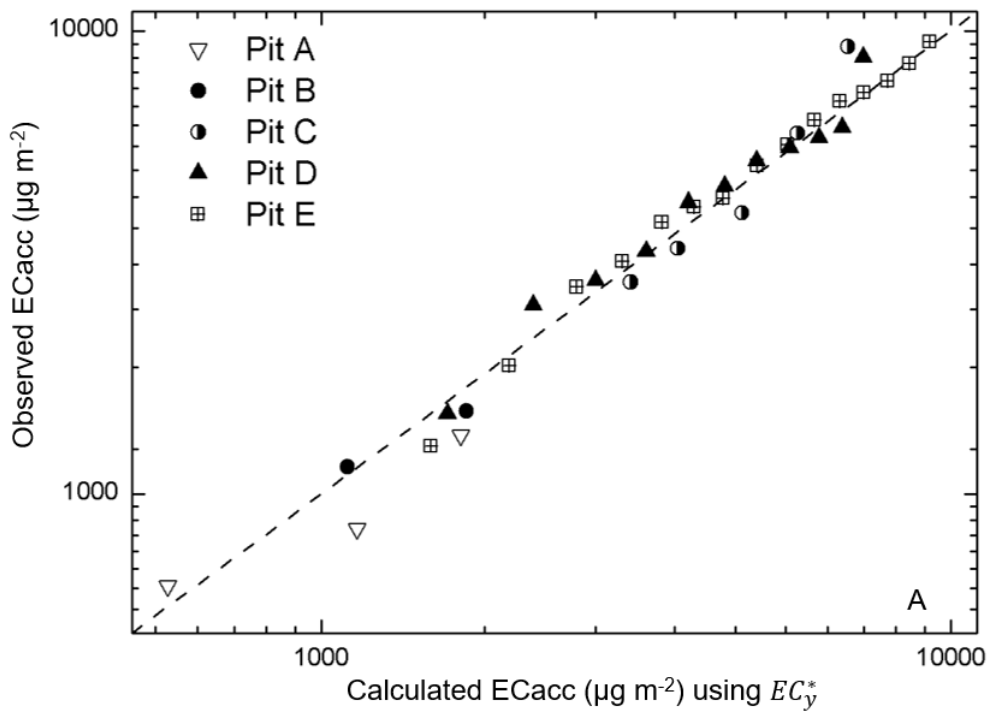


572 Figure 2. The cumulative \widehat{EC}_i (ECacc) from top to bottom in the snow pits as function of accumulated d_{SWEi} expressed as SWEacc (mm): (a) Pit A, (b) Pit B, (c)
573 Pit C, (d) Pit D, (e) Pit E, (f) Pit F. The upper dashed line represents a constant deposition EC_y^* and the lower dashed-dotted line represents a constant deposition
574 EC_o^* . In pit E there were no snow samples classified as old snow, hence there is no EC_o^* line, while in in pit F there were no young snow samples, therefore no
575 EC_y^* line.

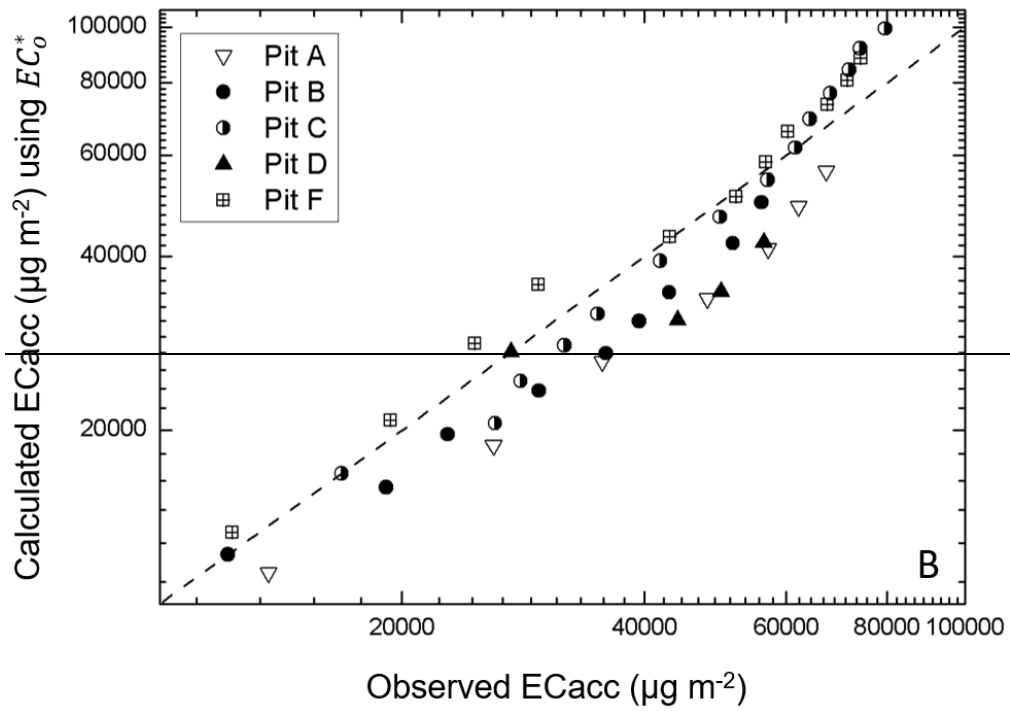
576



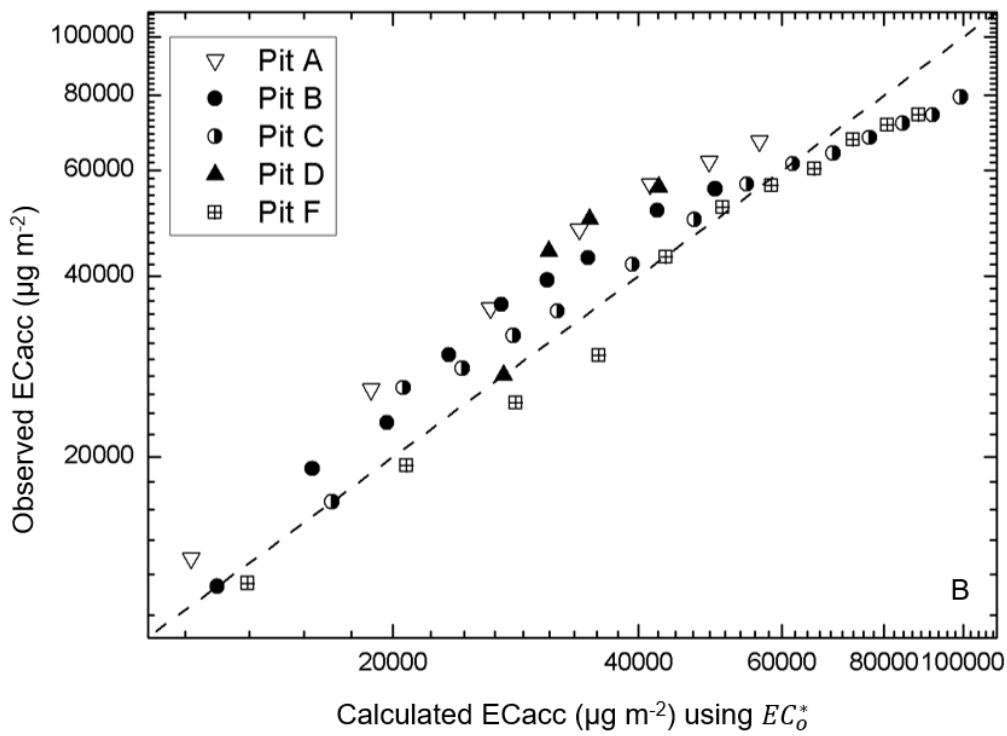
577



578



579



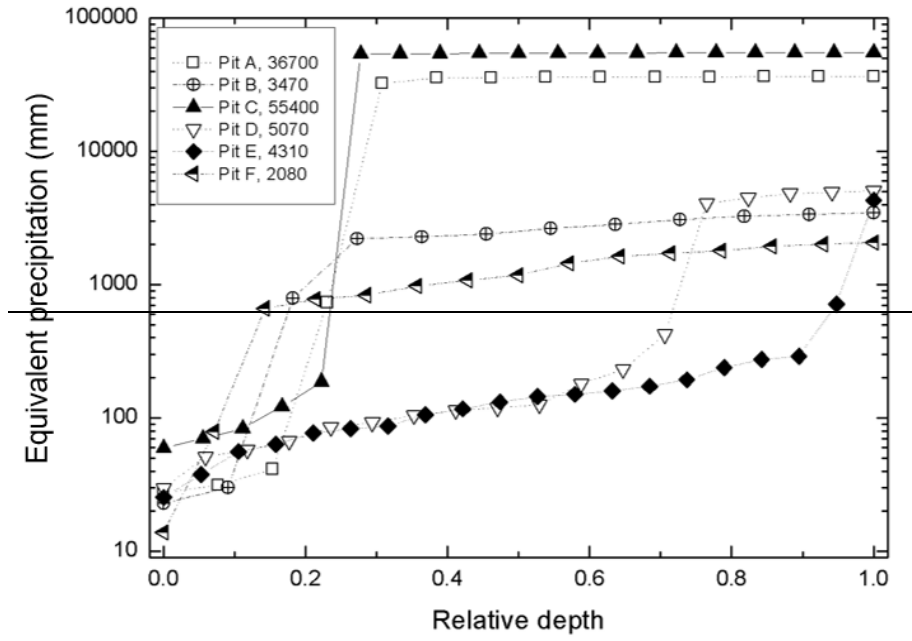
580

581 Figure 3. Observed and the calculated deposition using the constant deposition EC_y^* for young (a) and
 582 EC_o^* for old (b) snow samples. Dashed lines indicate a 1:1 slope.

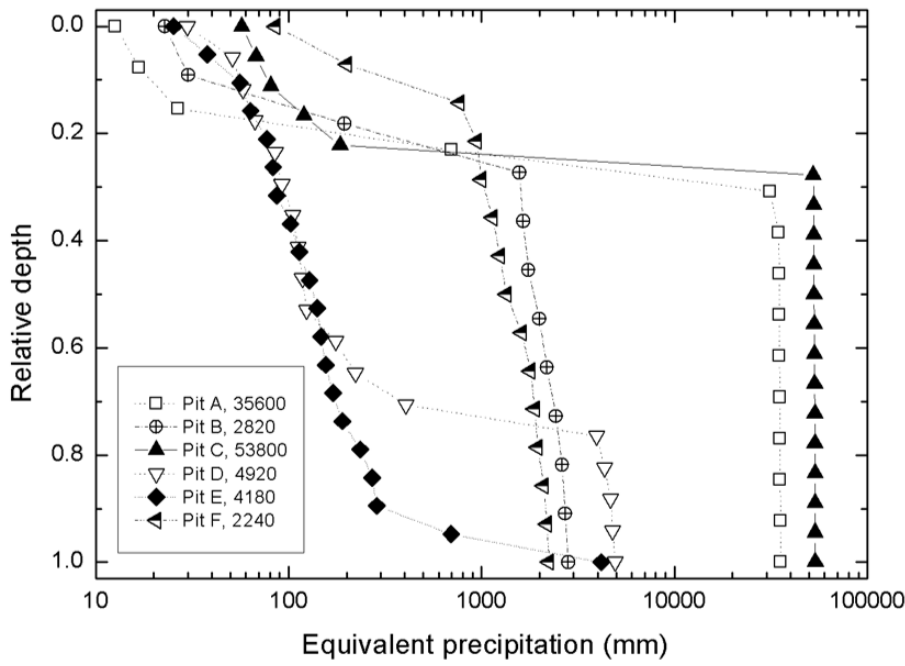
583

584

585



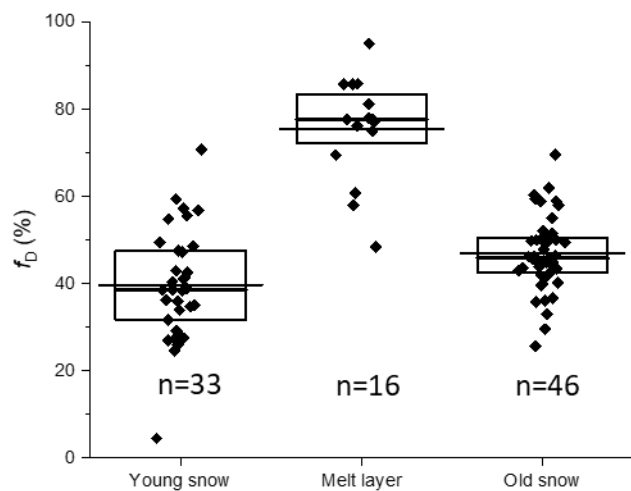
586



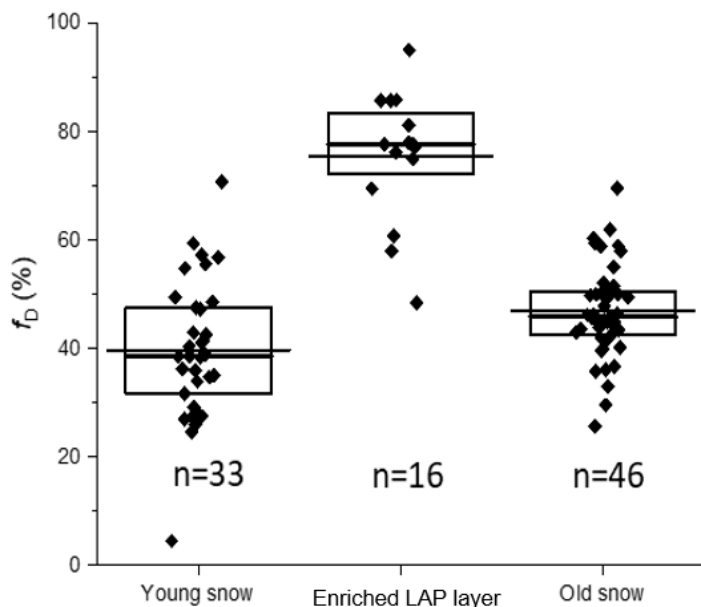
587

588 Figure 4. Equivalent precipitation for each pit based on a constant deposition EC_y^* in fresh snow as
 589 function of the relative depth of the pit from top to bottom.

590



591



592

593 Figure 5. Fractional dust absorption remaining after burning the filters during OC/EC analysis. The
 594 diamonds are individual values for each filter and the thin extended line represents the arithmetic
 595 average. The box and thicker line represent the quartile range and median, respectively. The number
 596 of samples are indicated in the figure as (n).